



# Compositional Maps of the Lunar Polar Regions Derived from the Kaguya Spectral Profiler and the Lunar Orbiter Laser Altimeter Data

Myriam Lemelin<sup>1,2</sup> , Paul G. Lucey<sup>3</sup> , and Alex Camon<sup>1</sup>

<sup>1</sup> Département de Géomatique appliquée, Université de Sherbrooke, Sherbrooke, QC, J1K 2R1, Canada; [Myriam.Lemelin@USherbrooke.ca](mailto:Myriam.Lemelin@USherbrooke.ca)

<sup>2</sup> Center for Lunar Science and Exploration, NASA Solar System Exploration Research Virtual Institute, USA

<sup>3</sup> Hawaii Institute of Geophysics and Planetology, University of Hawaii at Manoa, HI, USA

Received 2021 October 6; revised 2022 January 19; accepted 2022 February 7; published 2022 March 15

## Abstract

Due to the challenging illumination conditions of the lunar polar regions, mineralogic maps have generally been constrained to within 0°–70°N/S. Here we generate a gridded reflectance data cube from the Kaguya Spectral Profiler measurements for each polar region and calibrate it to absolute reflectance using data from the Lunar Orbiter Laser Altimeter. We use this data set to derive the first quantitative mineral maps of iron oxide (FeO), the optical maturity parameter (OMAT), and nanophase iron poleward of 50°N/S at a spatial resolution of 1 km pixel<sup>−1</sup>. We evaluate potential latitudinal trends in space weathering and optical maturity and characterize the polar geology, with an emphasis on the Artemis region (84°–90°S). The maps of FeO are in excellent agreement with the abundances measured by the Lunar Prospector and provide an increased level of detail, such as the excavation of high- and low-FeO material by De Forest crater. The OMAT maps offer a fantastic view of both polar regions. They highlight small fresh craters, walls, and central peaks, as well as rays extending through multiple degrees of latitude, such as those from Tycho and De Forest, which extend into the Artemis region. Both polar regions are characterized by the ubiquitous presence of noritic anorthosites and anorthositic norite. Low-calcium pyroxene is largely the dominant mafic mineral present. The Artemis region has relatively homogeneous FeO and plagioclase content at the observed spatial resolution. The lowest FeO values are found near Shackleton, between Shoemaker and Faustini, and on the central peak of Amundsen crater.

*Unified Astronomy Thesaurus concepts:* Planetary science (1255); Lunar surface (974); Lunar mineralogy (962)

## 1. Introduction

Estimating the mineralogical composition of the lunar surface from reflectance data acquired in the visible and near-infrared requires strong signal and well-calibrated reflectance values. The calibrated reflectance can, in turn, be used to compute the abundance of iron oxide (FeO) of a given spectrum to unambiguously define its composition based on its spectral shape and chemistry. Due to the poor illumination conditions in the polar regions, strong signal and well-calibrated reflectance data are scarce, and no sole instrument can meet these two critical requirements on the Moon. Thus, mineralogic maps have been constrained to within ~50° (e.g., Lemelin et al. 2015) or ~70° of the equator (e.g., Lucey 2004; Crites et al. 2015). The precise mineralogy of the polar regions, which corresponds to more than 16 million km<sup>2</sup> poleward of 50° in latitude, or ~44% of the lunar surface, is mostly unknown. A few studies have provided limited compositional analysis where strong absorption bands were present in order to identify the minerals present based on their spectral shape. These studies were constrained to individual detections of lithologies dominated by one or two minerals using Spectral Profiler or Moon Mineralogy Mapper data (e.g., Yamamoto et al. 2010, 2012; Haruyama et al. 2013; Kramer et al. 2013; Li et al. 2020). A few others investigated the position and strength of the 1 and 2 μm absorption band in the Moon Mineralogy Mapper data to evaluate the composition of pyroxenes in the South Pole–Aitken (SPA) basin (Moriarty & Pieters 2018;

Moriarty et al. 2020). To date, no comprehensive and quantitative polar mineral maps exist.

The International Space Exploration Coordination Group, a forum composed of 26 organizations, developed a Global Exploration Roadmap that provides a framework for coordinated efforts regarding robotic and human space exploration for years to come. Its latest version (ISECG 2018, 2020) presents a series of planned and upcoming robotic and human missions to the lunar surface from various international members. The NASA Commercial Lunar Payload Services program should, for example, send landers or rovers (e.g., the Volatiles Investigating Polar Exploration Rover) with a variety of instruments on board at a cadence of two missions per year starting in 2022, with the culmination of astronauts on the lunar surface a few years later. Other space agencies are actively involved in similar exploration missions. Many of the planned robotic missions aim to understand the science and exploration value of the lunar poles and will thus target the polar regions to land. These missions will begin with regional surveys (i.e., ground truth for ice, resources, and local chemistry at diverse locations), followed by site exploration of locations identified as high priority, which should ultimately support international sustained lunar surface activity (ISECG 2020). Deriving mineral maps of the polar regions using existing remote-sensing data sets would thus be highly beneficial for future lunar missions aiming to visit these polar regions, as knowledge of the mineralogy will likely influence the choice of landing sites and help design mission activities (e.g., sample material and/or primary crustal material).

In this study, we take a novel approach and use the strong signal and well-calibrated reflectance acquired by two different instruments, the Kaguya Spectral Profiler and the Lunar Orbiter



Original content from this work may be used under the terms of the [Creative Commons Attribution 4.0 licence](https://creativecommons.org/licenses/by/4.0/). Any further distribution of this work must maintain attribution to the author(s) and the title of the work, journal citation and DOI.

Laser Altimeter (LOLA), to derive polar mineral maps, as well as polar maps of FeO, the optical maturity parameter (OMAT), and nanophase iron in preparation for future missions. We generate a hyperspectral data cube from millions of Kaguya Spectral Profiler measurements. We use a reflectance ratio from the Spectral Profiler and calibrated reflectance data from the LOLA to derive polar maps of FeO and OMAT. We then use the Spectral Profiler reflectance data cube and Hapke radiative transfer model (e.g., Hapke 1981, 1993, 2001) to compute the abundance of olivine, low-calcium pyroxene, high-calcium pyroxene, and plagioclase using FeO as a constraint (Lemelin et al. 2015, 2019). Finally, we evaluate potential latitudinal trends in space weathering and optical maturity and characterize the polar geology, with an emphasis on the Artemis region ( $84^{\circ}$ – $90^{\circ}$ S).

## 2. Data Sets

The data sets used herein consist of data acquired by the Kaguya Spectral Profiler, the LOLA on board the Lunar Reconnaissance Orbiter mission, and the Lunar Prospector. We provide an overview of each of these data sets.

The Spectral Profiler acquired reflectance spectra of the surface between 500 and 2600 nm with an  $\sim 500$  m footprint (Haruyama et al. 2008). The instrument uses two gratings and three linear-array detectors: a visible detector (VIS, 500–1000 nm) and two near-infrared detectors (NIR1, 900–1700 nm; NIR2, 1700–2600 nm; Yamamoto et al. 2014). The radiometric calibration by Yamamoto et al. (2011) produced satisfactory results for VIS and NIR1 but was inadequate for NIR2; the method for removing the background resulted in noisy reflectance for NIR2 (Yamamoto et al. 2014). Consequently, data from VIS and NIR1 are mostly used in this paper. The profiler conducted continuous global spectral observations of the Moon in the visible to near-infrared region between 2007 and 2009. Thus, for most of the polar region, hyperspectral data were acquired at least once when the surface was illuminated in a given area. However, some crater walls facing the poles have low illumination (low signal-to-noise ratio), making mineralogical interpretation difficult. Here we used Spectral Profiler data at processing level 2B1, which contains radiometrically calibrated radiance data.

LOLA has been acquiring global observations of the Moon since 2009 and has the advantage of being an active sensor; it sends a laser pulse toward the Moon at 1064 nm and measures the energy backscattered from the surface regardless of the Sun's illumination conditions (Smith et al. 2010). It provides a high signal-to-noise ratio even on pole-facing slopes (i.e., it is not influenced by topography) and has been calibrated and gridded into polar maps of  $\sim 1$  km pixel $^{-1}$  by Lemelin et al. (2016). The LOLA data have also been used to model the polar illumination and identify permanently shaded regions (Mazarico et al. 2011). We used the location of permanently shaded regions (PSRs) poleward of  $65^{\circ}$ S at a spatial resolution of 240 m pixel $^{-1}$  (LPSR\_65S\_240M\_201608) derived from LOLA to investigate the latitudinal trend in space weathering and optical maturity.

The Lunar Prospector mission carried two instruments, a gamma-ray spectrometer and a neutron spectrometer, sensitive to the abundance of different elements, such as iron, in the lunar soil. Lawrence et al. (2002) used the data acquired by these two instruments to produce global maps of iron abundances at a spatial resolution of  $\sim 15$  km pixel $^{-1}$ . Here

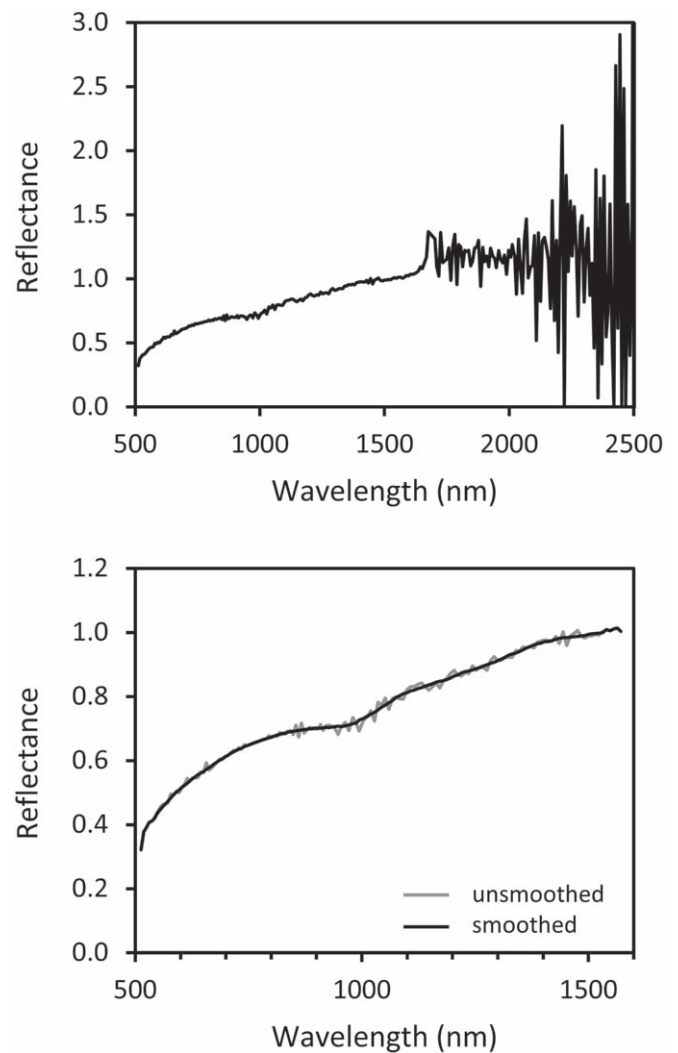


**Figure 1.** Reflectance calculated for a high-signal north polar point ( $85.716724^{\circ}$ N,  $112.59965^{\circ}$ W) in orbit 294. Top: data from all three SP detectors (VIS, NIR1, and NIR2). Bottom: data extracted for this study (VIS and NIR1).

we use the Lunar Prospector iron abundances to validate the FeO abundances derived herein using the Spectral Profiler and LOLA.

## 3. Methods

Production of FeO and mineral maps at midlatitudes takes advantage of the calibration of the radiance data into absolute reflectance, including correction for the effect of topography on the signal (e.g., Lemelin et al. 2015, 2019). In the polar regions, grazing illumination on level surfaces leads to poor signal-to-noise ratios. However, polar Sun-facing surfaces such as crater rims are more directly illuminated and do feature high signal-to-noise ratios. Owing to the drastic variation in lighting influenced by topography, derivation of absolute reflectance is challenging at these latitudes, preventing the use of the previous algorithms. We solve this problem by selecting high-signal portions of the polar data set and normalizing these spectra to their 1064 nm wavelength. We then use the polar absolute reflectance collected by the active LOLA instrument to renormalize the spectra to absolute reflectance, appropriate to apply mineral and elemental abundance algorithms.



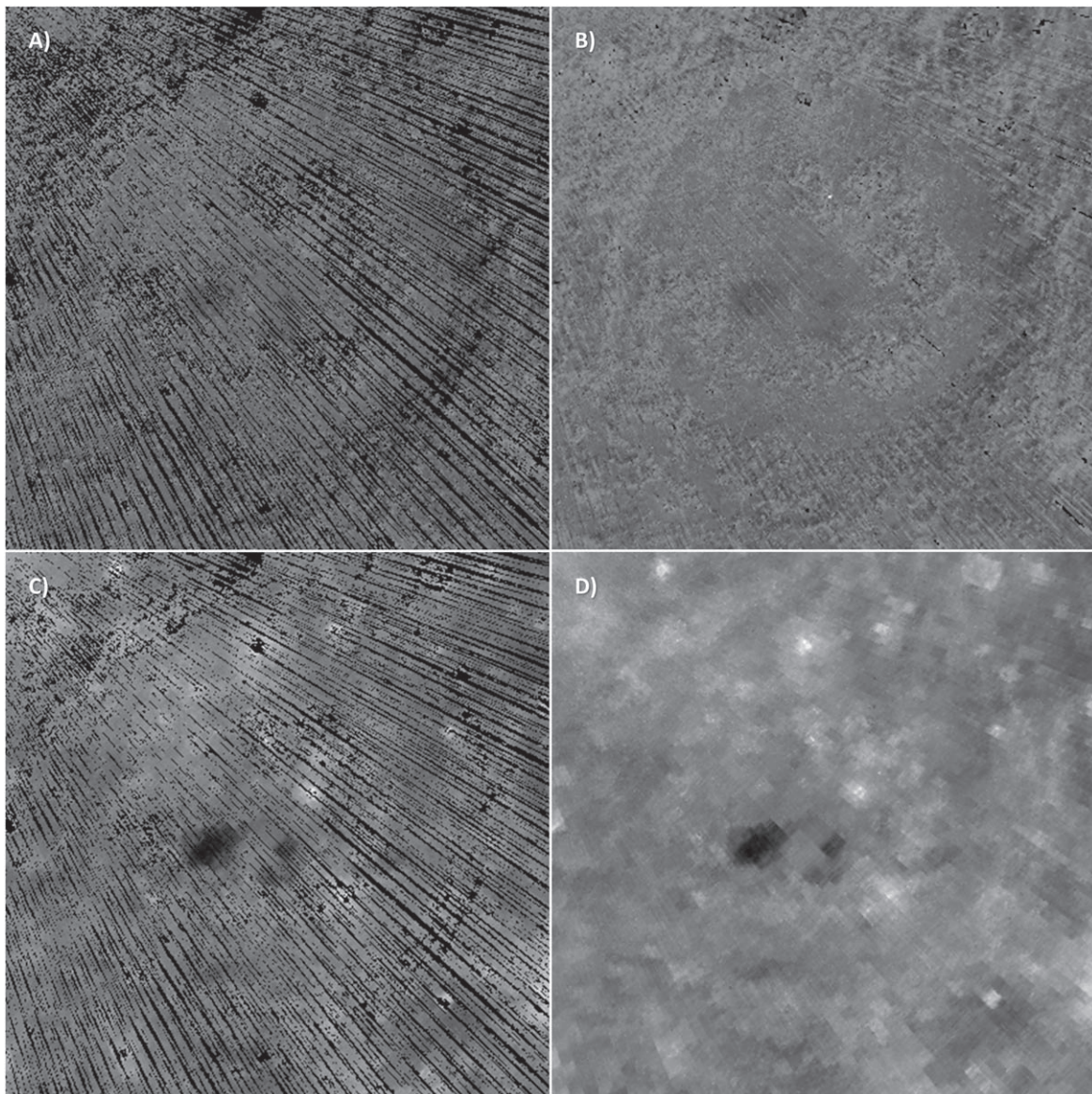


**Figure 2.** Different gridded data products for Schrödinger crater. (a) Gridded Spectral Profiler 1064 nm reflectance data showing the location and spatial density of spectral measurements. (b) Interpolated data. (c) Spectral Profiler 1064 nm reflectance data scaled to the LOLA 1064 nm reflectance data. (d) Interpolated data. Variations in reflectance due to topography are removed.

The methods used herein thus include (1) the preprocessing of Spectral Profiler data to generate a bidirectional reflectance distribution function (BRDF) data cube at visible and near-infrared wavelengths, (2) the use of this data cube and LOLA gridded data to derive new polar FeO and OMAT algorithms, and (3) the use of this data cube along with radiative transfer modeling to calculate polar minerals and maps of nanophase iron abundances.

### 3.1. Preprocessing of Spectral Profiler Data

The overarching goal of the Spectral Profiler preprocessing is to generate a reflectance data cube for each polar region that contains nonnoisy reflectance data in a maximum of wavelengths. To do so, we first converted the Spectral Profiler radiance data measured in each of the  $\sim 7000$  orbits into the BRDF using the photometric function of Yokota et al. (2011). This allowed for calculating the reflectance value to a standard viewing geometry of  $30^\circ$  incidence angle ( $i$ ),  $0^\circ$  emission angle

( $e$ ), and  $30^\circ$  phase angle ( $\alpha$ ) for all Spectral Profiler data points acquired in the polar regions. The photometric function of Yokota et al. (2011) assumes the surface is flat. Therefore, sloped surfaces can have a higher or lower BRDF than expected. Therefore, we recommend using the absolute values of the gridded BRDF data cube with caution or relying on band ratios or continuum-removed spectra for further analysis, which minimizes the effect of the slope of the BRDF measurements. For simplification, for the rest of the paper, we will call “reflectance” the BRDF values calculated using the Yokota et al. (2011) parameters. We then selected the valid measurements to be included in the reflectance data cube. We calculated the signal-to-noise ratio for all spectra as the amplitude of variations in contiguous spectral bands divided by its standard deviation for wavelengths between 750 and 1550 nm (which excludes the high noise in the NIR2 data). We established the validity cutoff as spectra with a signal-to-noise ratio greater than 50 and radiance greater than



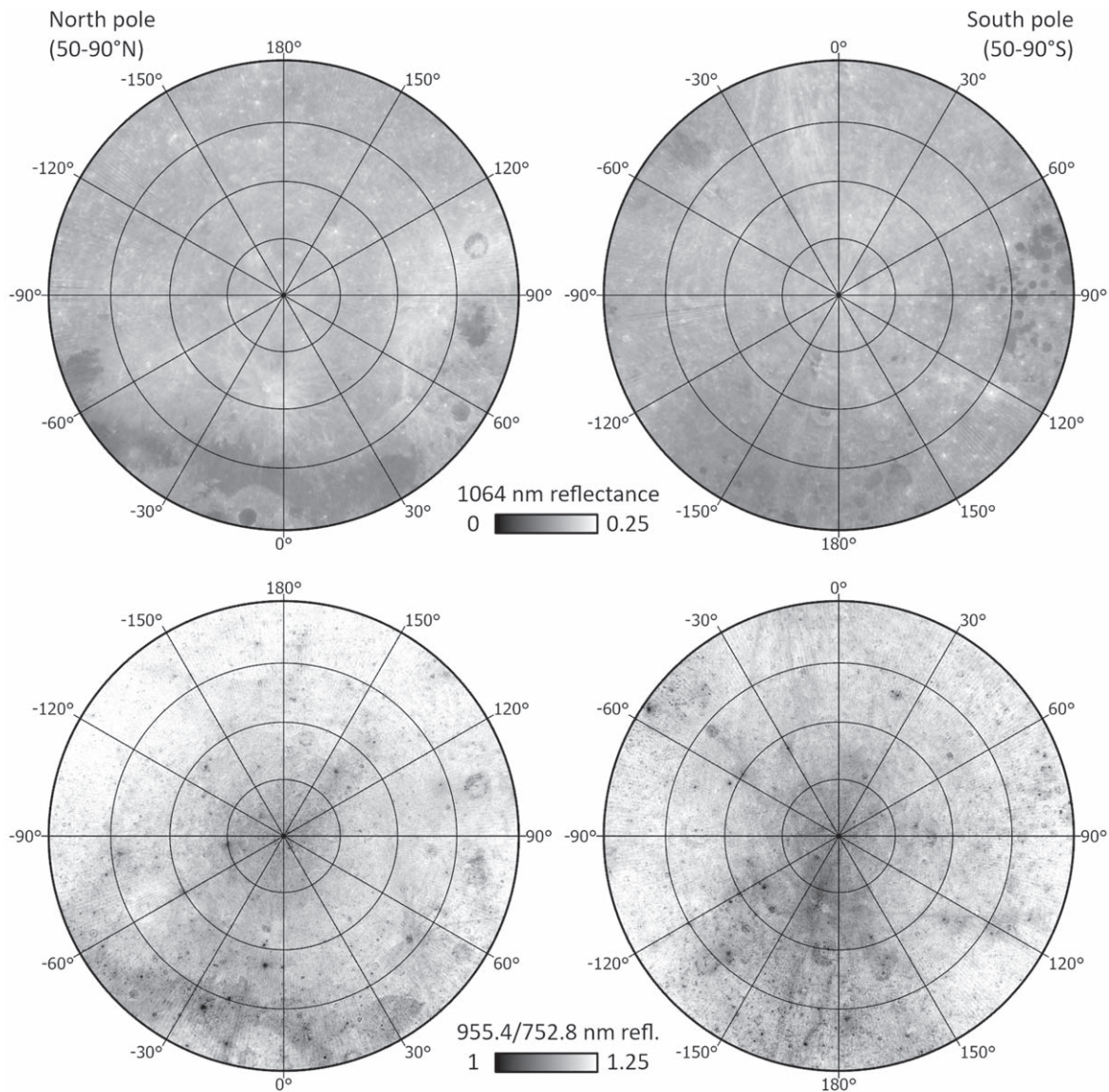


**Figure 3.** Calibrated Spectral Profiler 1064 nm reflectance and 955.4/752.8 nm reflectance ratio for both polar regions. Low Spectral Profiler ratios are mostly associated with less optically mature surfaces and surfaces containing higher iron abundances. High 1064 nm reflectance is mostly associated with surfaces containing low iron abundances and less optically mature surfaces.

$50 \text{ W m}^{-2} \text{ sr}^{-1} \mu\text{m}^{-1}$  at 752.8 and 955.4 nm (the bands used in the FeO algorithm). This left approximately 9 million spectra in each (north and south) polar region. Spectral measurements with a signal-to-noise ratio greater than 50 contain abundant noise in the wavelengths covered by the NIR2 detector (1700–2600 nm; Yamamoto et al. 2014, Figure 1). We thus only used the data acquired by the VIS detector and part of the NIR1 detector away from that noise, between 512.6 and 1571.7 nm. We removed the measurements acquired at the overlapping wavelengths by the two detectors, which results in a total of 150 spectral bands. We smoothed each spectrum individually before the gridding process with a boxcar average of 10 reflectance values in contiguous wavelengths (Figure 1).

Once the  $\sim 18$  million spectral measurements have been filtered and smoothed individually, we generated a spectral data cube for each polar region. We built a polar stereographic projection grid with a spatial resolution of  $1000 \text{ m pixel}^{-1}$  (true at the pole) and averaged all measurements acquired within each pixel (Figure 2). We calculated a count map to inform on

the density of measurements within each pixel. We then scaled the reflectance of each pixel to that of the scaled LOLA data (Lemelin et al. 2016). This process involves a two-step procedure: (1) reconcile the LOLA and Spectral Profiler viewing geometry and (2) scale the Spectral Profiler reflectance to the polar LOLA data. The reflectance measurements provided by the Spectral Profiler and LOLA have been acquired at different phase angles; the Spectral Profiler reflectance measurements have been calibrated to a standard viewing geometry of  $i = 30^\circ$ ,  $e = 0^\circ$ , and  $\alpha = 30^\circ$ , whereas the LOLA reflectance measurements have a viewing geometry of  $i = e = \alpha = 0^\circ$ . Since the Moon is not a Lambert surface (an ideal surface that reflects light equally in all directions) and features a strong opposition effect, its reflectance at  $\alpha = 0^\circ$  is much greater than its reflectance at  $\alpha = 30^\circ$  (Barker et al. 2016). By computing the offset in reflectance between the Spectral Profiler and LOLA data at the same wavelength (1064 nm) and applying that offset to the LOLA data, we can convert it to the same standard viewing geometry of  $i = 30^\circ$ ,  $e = 0^\circ$ ,

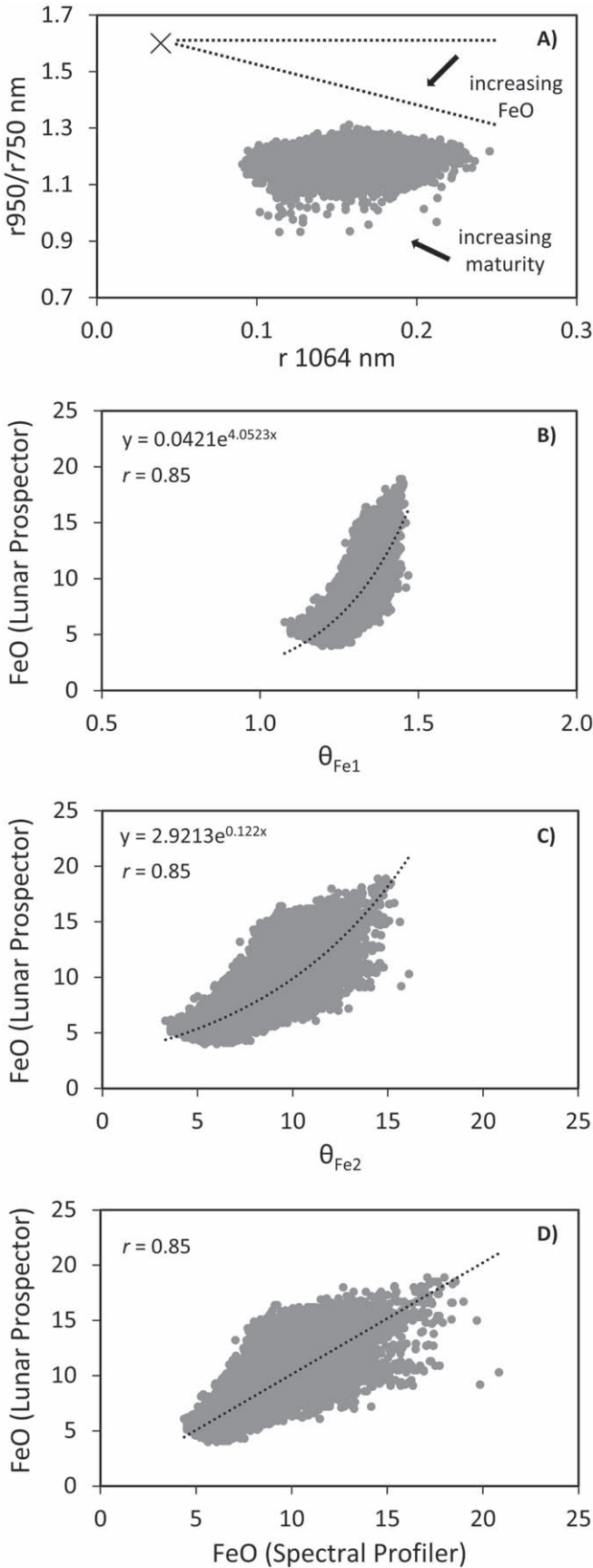


**Figure 4.** Derivation of the polar FeO algorithm using Spectral Profiler and Lunar Prospector gridded data between  $50^\circ$  and  $90^\circ$ N/S at a spatial resolution of  $15 \text{ km pixel}^{-1}$ .

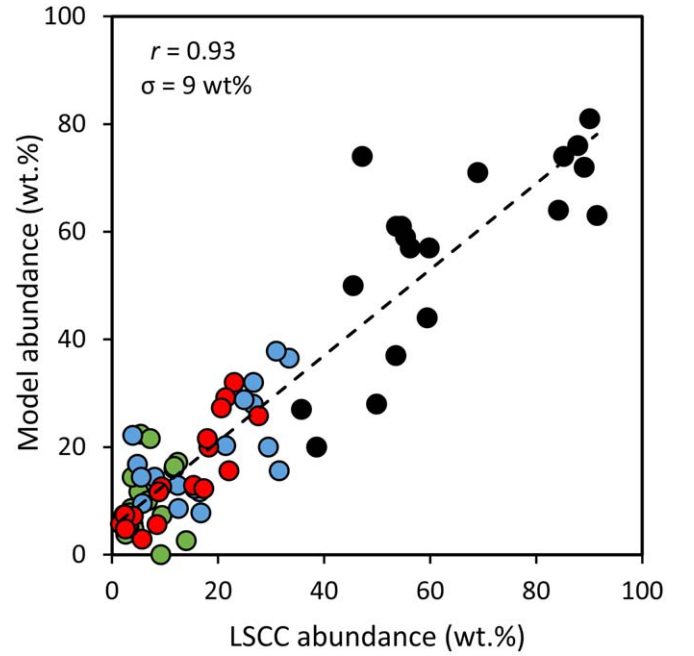


**Figure 5.** Error in mineral abundance between our model and the mineral abundances measured by the LSCC. The model uses the refined optical constants of Lucey (1998) to minimize the difference in mineral abundances between our model and the LSCC data. The comparison uses Spectral Profiler wavelengths between 746.8 and 1555.5 nm. Olivine is shown in green, low-calcium pyroxene in blue, high-calcium pyroxene in red, and plagioclase in black. The correlation ( $r$ ) between the two data sets is 93%, and the rms error in mineral abundance estimation is 9 wt%.

and  $\alpha = 30^\circ$ . To find the appropriate scaling factor, we created a  $1 \text{ pixel deg}^{-1}$  equatorial mosaic of both LOLA and the Spectral Profiler at 1064 nm reflectance. The Spectral Profiler instrument does not have a 1064 nm band, so we averaged the measurements in the two closest wavelengths (1060 and 1068 nm; Equation (1)). We computed their respective histograms using data within  $\pm 50^\circ$  in latitude, far from the bias that could be introduced due to topography in the Spectral Profiler data, and performed a histogram matching, varying the gain until a minimal difference between the two histograms is reached. That gain (0.56) can then be applied to the LOLA reflectance data in the polar region (Equation (2)) to provide calibrated reflectance measurements at a standard viewing geometry of  $i = 30^\circ$ ,  $e = 0^\circ$ , and  $\alpha = 30^\circ$ . This reflectance difference is consistent with the study of lunar photometric properties at 1064 nm by Barker et al. (2016):

$$r_{1064(\text{SP})} = (r_{1060(\text{SP})} + r_{1068(\text{SP})})/2, \quad (1)$$

$$r_{1064(\text{LOLA scaled})} = r_{1064(\text{LOLA})} \cdot 0.56. \quad (2)$$

The second step is to scale the Spectral Profiler reflectance to the scaled polar LOLA data. To do so, we applied a gain to the gridded Spectral Profiler reflectance data in all wavelengths so that its 1064 nm measurements match the scaled LOLA data in all pixels (i.e., the gain is pixel-dependent). Scaling the gridded Spectral Profiler measurements to the scaled gridded LOLA data normalizes effects introduced by topography in the Spectral Profiler BRDF calculation and allows one to produce a calibrated gridded Spectral Profiler data cube. We then used a bilinear interpolation method to interpolate the missing measurements using a moving window size dependent on the number of neighboring measurements available (Figure 2).



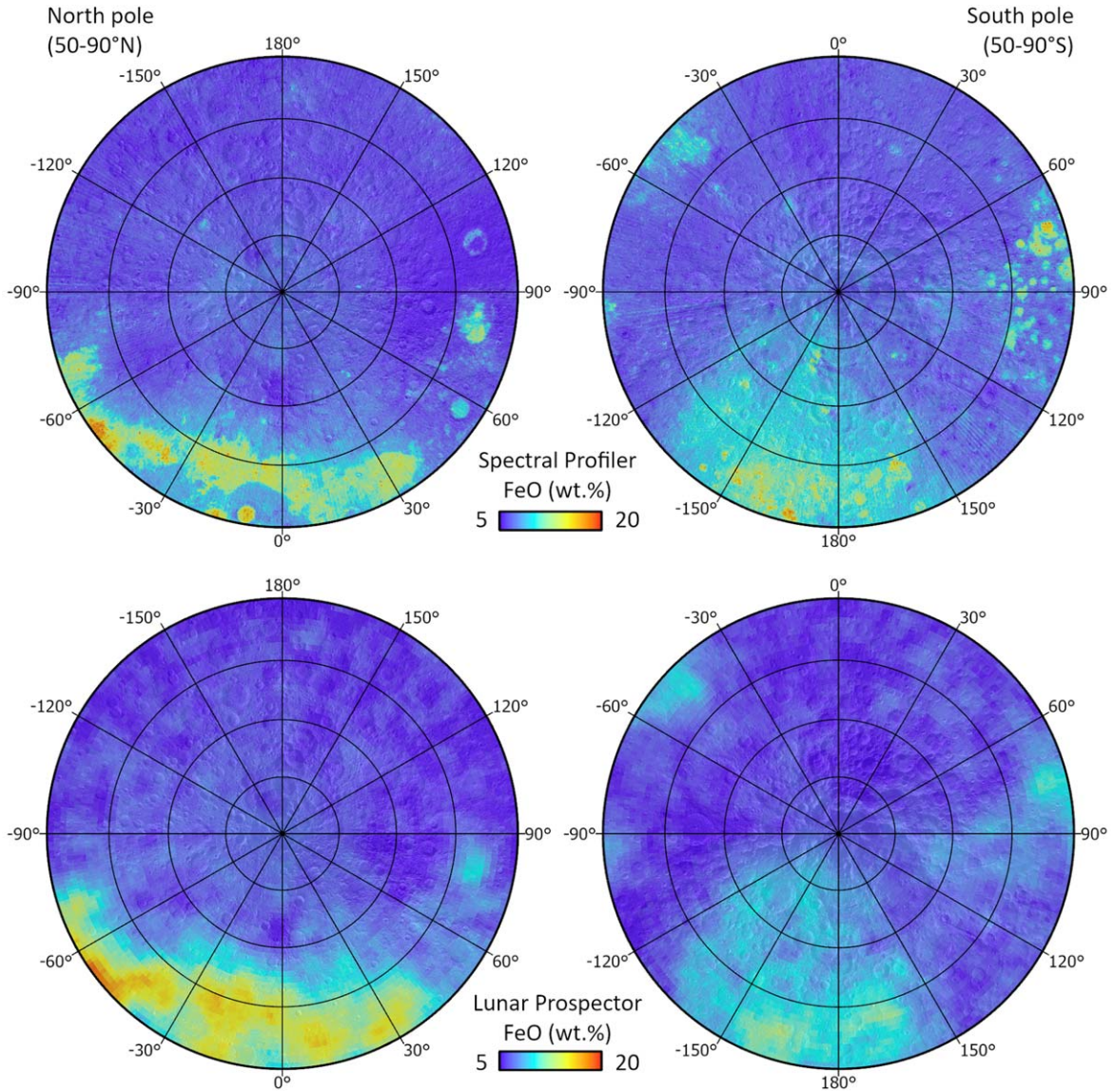


**Figure 6.** North and south polar maps of FeO abundance. Top: calibrated Spectral Profiler data at 1 km pixel<sup>-1</sup>, Bottom: Lunar Prospector data at 15 km pixel<sup>-1</sup>. The data are shown in polar stereographic projection between 50°–90°N (left) and 50°–90°S (right) in latitude with 20% transparency over the Wide Angle Camera global mosaic.

### 3.2. Calculating FeO Abundances

Lucey et al. (1995) introduced a method for the estimation of the iron content of the lunar surface using the reflectance in the visible wavelength (VIS, 750 nm) and the ratio of reflectance in the near-infrared over visible wavelengths (NIR, 950 nm; VIS, 750 nm). They noted trends related to iron content and optical maturity (the optical effects of space weathering) on a plot of the NIR/VIS ratio versus the VIS reflectance for returned lunar samples and defined an angular parameter using the sample location in that plot. They used the relationship between the iron content of the samples and the spectral parameter to provide a transformation from remotely sensed spectral information to iron content, normalizing the effects of space weathering. Lucey et al. (2000) presented this method using reflectance data from the Clementine mission in the equatorial region. Lemelin et al. (2015) used this method to derive similar equations for the calculation of iron from the Kaguya Multiband Imager data. Such a method requires precisely calibrated reflectance data, which we produced for the polar region using the above method.

To derive an FeO algorithm for the lunar polar regions using the approach of Lucey et al. (2000), we used the calibrated Spectral Profiler data cube. We use the reflectance at 955.4 and 752.8 nm to derive the reflectance ratio and the reflectance at 1064 nm (Equation (1)). We use the abundance of FeO measured by the Lunar Prospector Gamma-Ray Spectrometer (Lawrence et al. 2002) to validate the FeO abundances derived herein. We resampled all data sets to a common spatial resolution of 15 km pixel<sup>-1</sup>. We first plotted the 955.4/752.8 nm ratio versus the 1064 nm reflectance and determined which optimized origin would maximize the correlation between  $\theta_{\text{Fe1}}$  and Lunar Prospector FeO (Figures 3(a) and (b)). This new optimized origin is  $x_{0\text{Fe}} = 0.04$  and  $y_{0\text{Fe}} = 1.60$  (Equation (3)). An exponential curve is used to derive  $\theta_{\text{Fe2}}$  (Equation (4)), and another exponential curve is used to derive FeO from  $\theta_{\text{Fe2}}$  (Figure 4, Equation (5)):

$$\theta_{\text{Fe1}} = -\arctan \left\{ \frac{[(r_{955.4}/r_{752.8}) - y_{0\text{Fe}}]}{(r_{1064} - x_{0\text{Fe}})} \right\}, \quad (3)$$

$$\theta_{\text{Fe2}} = 0.0421e^{4.0523\theta_{\text{Fe1}}}, \quad (4)$$

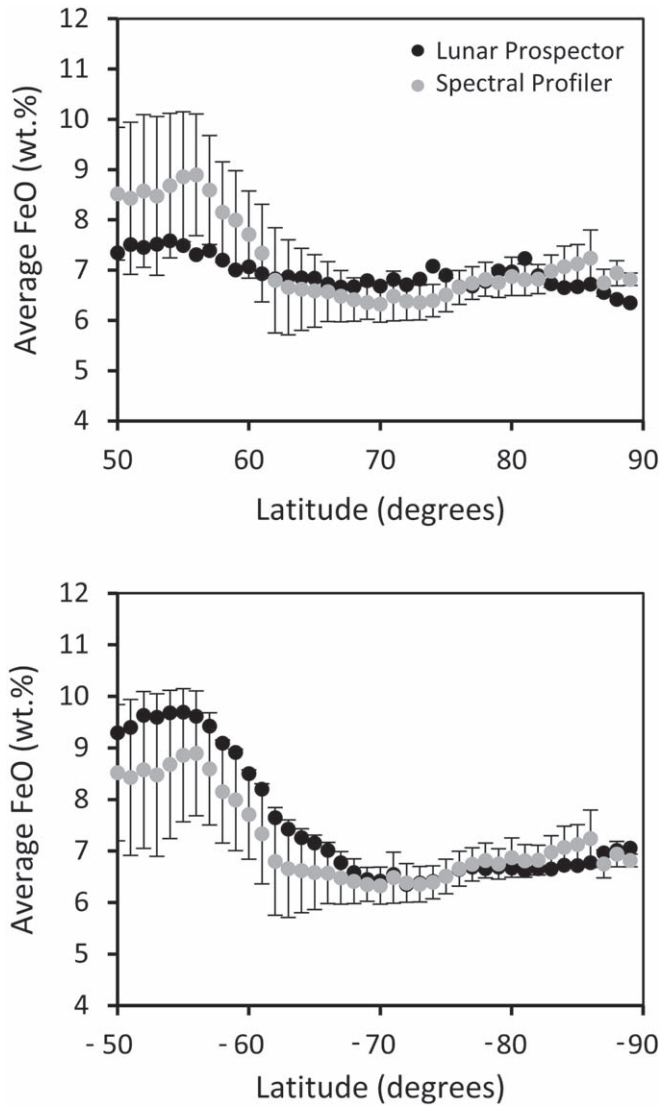


**Figure 7.** Average FeO by latitude for Lunar Prospector and Spectral Profiler data at 15 km pixel<sup>-1</sup>. The error bars represent plus or minus one standard deviation from the Spectral Profiler FeO abundances.

$$\text{FeO (wt.\%)} = 2.9213e^{0.122\theta_{\text{FeO}}}. \quad (5)$$

#### 4. Deriving the OMAT

With exposure to space, the lunar surface chemically and physically changes. The process leading to these changes is called maturation, and the degree to which a soil possesses quantitative characteristics consistent with that maturation is termed maturity (Morris 1978). Some of the physical changes caused by maturation lead to changes in the optical characteristics of soils. As soils mature, their spectra become darker and redder, and their spectral contrast is reduced. Lucey et al. (1995, 1998, 2000) developed the OMAT parameter to quantify this optical maturation using the 750 and 950/750 nm reflectance data of returned Apollo soil samples and generate near-global OMAT maps from Clementine data. The Clementine OMAT maps were restricted to latitudes within 70°, where the Clementine data calibration was optimal. Lemelin et al. (2019) derived a similar algorithm to be used with the Kaguya Multiband Imager data, which were best calibrated within 50° of latitude. Here we modify the algorithm of

Lucey et al. (2000) to be used with our calibrated Spectral Profiler polar data set. We use the optimized origin (hypermaturation end-member) defined in the FeO algorithm above and the calibrated Spectral Profiler 955.4/752.8 nm reflectance ratio and 1064 nm reflectance (Equation (6)):

$$\text{OMAT} = \left[ (r_{1064} - x_{0\text{Fe}})^2 + \left( \left( \frac{r_{955.4}}{r_{752.8}} \right) - y_{0\text{Fe}} \right)^2 \right]^{\frac{1}{2}}. \quad (6)$$

#### 5. Modeling Mineralogy

We derive the mineralogical composition of the lunar surface using visible and near-infrared wavelengths by comparing reflectance spectra to modeled spectra of known composition and assigning the composition of the best spectral match. Radiative transfer equations, which describe the scattering of light interacting with surfaces, allow for modeling reflectance spectra of mineral mixtures for various grain sizes, chemistry, and space weathering effects. As different compositions can have similar spectra, iron abundance can be used as a constraint to mitigate uncertainties (Lemelin et al. 2015, 2019). In this study, we use Hapke's radiative transfer equations (e.g., Hapke 1981, 1993, 2001) and the approach described in Lemelin et al. (2015, 2019) to derive compositions from the gridded polar reflectance mosaics produced in Section 3.1. We use Hapke's radiative transfer equations to compute a spectral library corresponding to mixtures of olivine, low-calcium pyroxene, high-calcium pyroxene, and plagioclase at Spectral Profiler wavelengths between 746.8 and 1555.5 nm, the same wavelength range studied by Lemelin et al. (2015, 2019). We compare the spectra of each pixel against the spectral library and assign the composition to the best spectral match, using FeO as a constraint. Further details concerning each step are presented below.

The spectral library used herein contains the same mineral mixtures as derived by Lemelin et al. (2015, 2019) for the Multiband Imager wavelengths; it contains relative abundances of the mafic minerals at 10% intervals and a relative abundance of plagioclase at 1% intervals for a total of 6601 different compositions. The exposure of the lunar surface to space leads to important modifications of its physical properties, i.e., space weathering, which leads to important modifications in the spectral quantities measured. A vapor coating is deposited on soil grains by solar wind sputtering and micrometeorite impact vaporization, and metallic iron particles smaller than the wavelength are reduced and implanted in this coating by the selective loss of oxygen that occurs during vapor deposition (Hapke 2001). These physical and chemical changes lead to spectral darkening, reddening, and subdued absorption bands characteristic of each mineral and need to be accounted for in quantitative mineral analysis. Optically small nanophase iron is responsible for the reddening and a portion of the observed darkening of the lunar soil (Hapke 2001; Noble et al. 2007; Lucey & Noble 2008), while microphase iron is responsible for the observed darkening (Britt & Pieters 1994; Noble et al. 2007; Lucey & Riner 2011). Here we compute the mineral mixtures at 11 different amounts of nanophase iron. Nanophase iron varies between 0.37 and 1 wt.%, for a total of 72,611 modeled spectra. We fix the molar MgO/(MgO+FeO) (Mg#) at 65 (representative of the more magnesian of the ferroan anorthosites) and a grain size of 17 μm for all minerals (Pieters et al. 1993; Lucey 2006). We use the optical constants



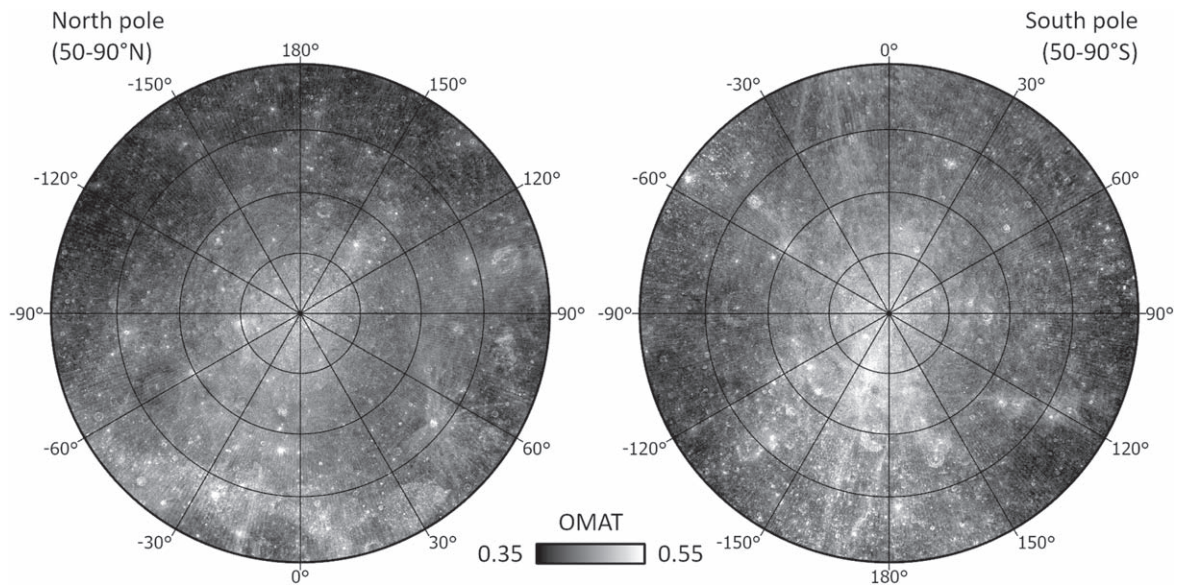


**Figure 8.** North and south polar maps of OMAT. The data are shown in polar stereographic projection between 50°–90°N (left) and 50°–90°S (right) in latitude.

of Lucey (1998) and adjust them so that they provide the best agreement between the mineral abundances measured by the Lunar Soil Characterization Consortium (LSCC) for 19 lunar soil samples of 10–20  $\mu\text{m}$  in particle size (Taylor et al. 2001) and our model at the Spectral Profiler wavelengths. Lucey et al. (2014) showed that there is a poor correlation of the model and measured mineralogy (25 wt.% error) when using the optical constants of Lucey (1998) as is. Olivine is overestimated, and the modeled spectra do not match the trend of band minimum versus the ratio of low-calcium pyroxene to the total abundance of pyroxene. As done by Lucey et al. (2014) for the Multiband Imager wavelengths, we perform a grid search, changing the intensity of the imaginary index spectrum for olivine and plagioclase and the position of the imaginary index spectrum minimum for the pyroxenes. We find that increasing the intensity of the imaginary index spectrum for olivine by a factor of 5 and plagioclase by a factor of 1.7 and shifting the position of the imaginary index spectrum minimum for low-Ca pyroxene by 15 nm to shorter wavelengths and 55 nm to longer wavelengths for high-Ca pyroxene provide the best agreement between the LSCC and the modeled mineral abundances. These modified optical constants, similar to those found by Lucey et al. (2014), yield an error (RMSE) of 9 wt.% in mineral abundance at the Spectral Profiler wavelengths (Figure 5).

To assign a mineralogical composition to a Spectral Profiler spectrum, we remove a continuum (a straight line tangential to the reflectance spectrum at 746.8 and 1555.5 nm) from the library spectra and the given Spectral Profiler spectrum and find the closest spectral match (using an evenly weighted average of the correlation between the library and the unknown spectrum and the sum of the absolute difference in reflectance between the library and the given pixel spectrum). Because reflectance spectra of different compositions can be similar in shape, we use the abundance of FeO as a constraint. We compute the FeO abundance consistent with the stoichiometric abundance of each mineral mixture in the spectral library and use the FeO map described above. Only the library spectra that have  $\pm 2$  wt% of the FeO content of a given spectrum are compared.

## 6. Results

### 6.1. FeO

The abundance of FeO obtained using the calibrated Spectral Profiler data and the equations herein are in agreement with the abundance of FeO measured by the Lunar Prospector Gamma-Ray Spectrometer (Figure 4;  $r = 0.85$ ,  $\sigma = 1.41$ , RMSE = 1.41). Figure 6 presents the FeO obtained using the calibrated Spectral Profiler data and the algorithm herein at a spatial resolution of 1 km pixel<sup>-1</sup> and the FeO measured by the Lunar Prospector data at 15 km pixel<sup>-1</sup>. As expected, the FeO derived herein provides an increased level of detail while preserving the regional observations from the Lunar Prospector. High-FeO anomalies are seen in the maria, while De Forest crater (77°3S, 162°1W) appears to have excavated both high- and low-FeO material. Low-FeO anomalies are seen for three large craters in the north polar region, which can also be seen in the Lunar Prospector data. Figure 7 presents the average FeO abundances by latitude measured by each technique when both data sets are resampled to a spatial resolution of 15 km pixel<sup>-1</sup>. The largest difference (on average,  $\sim 1$  wt.%) between the Lunar Prospector and Spectral Profiler FeO is observed between 50° and 60°N/S. Values poleward of 60°N/S generally have a difference in FeO < 1 wt.% (Figure 7).

### 6.2. Optical Maturity Parameter

The new OMAT product calculated herein offers a fantastic view of both polar regions as never seen before (Figure 8). The OMAT maps highlight small fresh craters and the fresh walls and central peaks of larger craters, as well as rays extending through multiple degrees of latitude, such as those from Tycho and De Forest. We note that the polar OMAT values derived from the calibrated Spectral Profiler data are significantly higher (average  $\sim 0.4$ ) than those calculated using Clementine or the Multiband Imager data in the equatorial region (average  $\sim 0.2$ ). This is primarily due to the different optimized origins used, as well as to the fact that the polar regions are less affected by space weathering caused by solar wind (Hemingway et al. 2015; Lemelin et al. 2016). The absolute



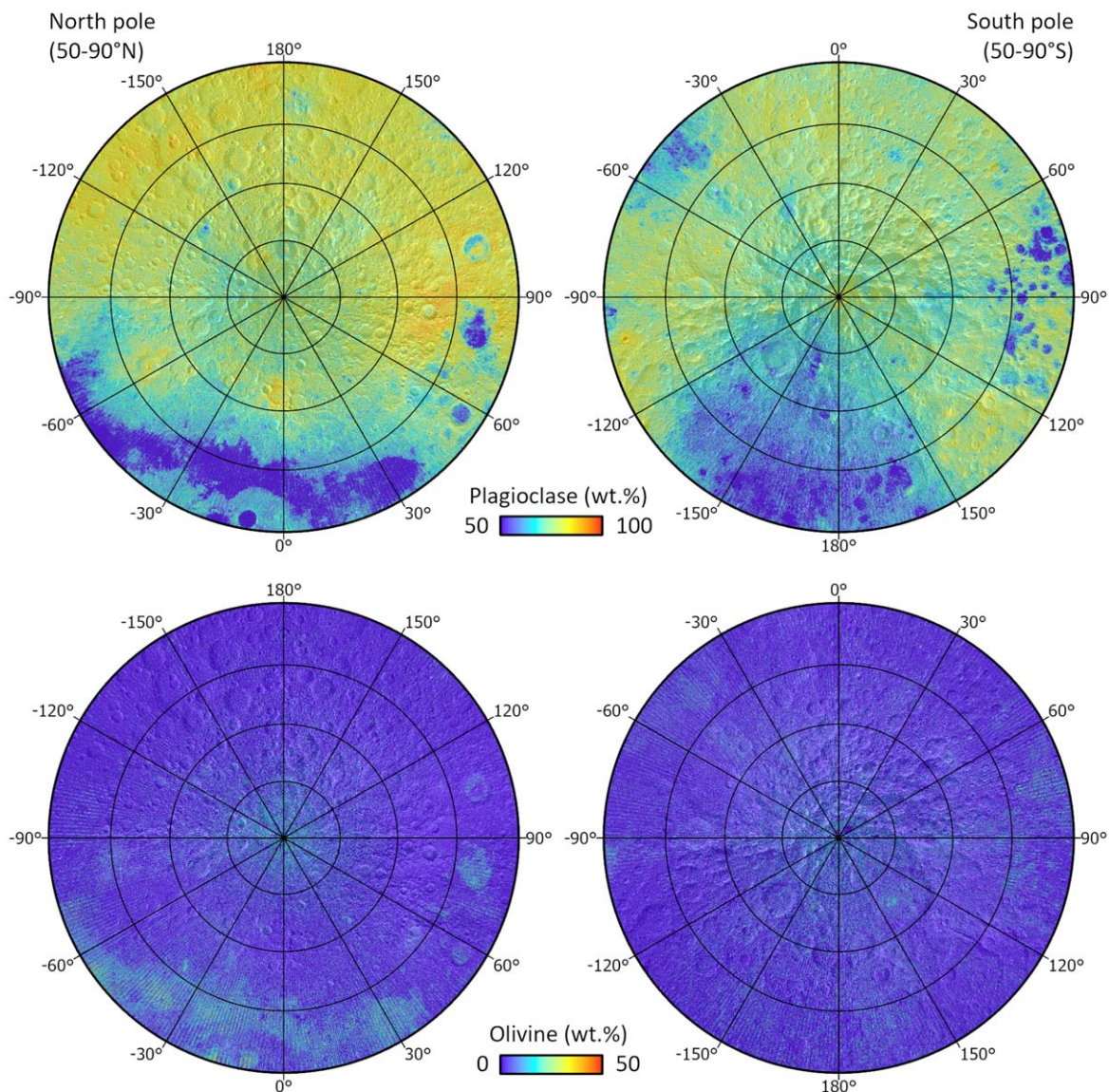


**Figure 9.** North and south polar maps of plagioclase and olivine abundances. The data are shown in polar stereographic projection between 50°–90°N (left) and 50°–90°S (right) in latitude with transparency over the Wide Angle Camera global mosaic.

OMAT values derived from different data sets should thus be used with caution, considering an offset between both values.

### 6.3. Minerals

The abundance of plagioclase in the north polar region is representative of the dominance of noritic/gabbroic anorthosite or troctolitic anorthosite (77.5–90 wt.% plagioclase) followed by anorthositic norite/gabbro or anorthositic troctolite (60–77.5 wt.% plagioclase) (Figure 9). Exposures of norite/gabbro, olivine norite/gabbro, or troctolite (10–60 wt.% plagioclase) are generally restricted to Mare Frigoris, Mare Humboldtianum, the mare-infilled Endymion crater (53°9N, 57°E), and a few other small locations. Exposures of anorthosites (90–100 wt.% plagioclase) are mostly concentrated in the region in and around the complex craters Hayn (64°7N, 85°2E), Compton (55°3N, 103°8E), and Schwarzschild (70°1N, 121°2E). Other exposures are sparsely found, such as in the Birkhoff region (58°7N, 146°1W).

The south polar region is characterized by the dominance of anorthositic norite/gabbro or anorthositic troctolite (60–77.5 wt.% plagioclase) followed by noritic/gabbroic anorthosite or troctolitic anorthosite (77.5–90 wt.% plagioclase) (Figure 9). Exposures of norite/gabbro, olivine norite/gabbro, or troctolite (10–60 wt.% plagioclase) are found in SPA, Mare Australe, the Schiller–Zucchi basin (56°S, 45°W), and a few other small locations. Exposures of anorthosites (90–100 wt.% plagioclase) are rarer in the south polar region than in the north polar region. A few are concentrated around Shackleton crater (89°9S) and on or near the ridge between Shackleton and Henson craters (~88°5S, 128°W). Other exposures are sparsely distributed.

In both polar regions, low-calcium pyroxene is largely the dominant mafic mineral present (Figure 10). It appears to be the dominant mafic mineral in all mare exposures and in the highlands. High-calcium pyroxene and olivine are present in much lower abundances and generally restricted to mare exposures and the center of SPA (Figure 10). The ubiquitous dominance of low-calcium pyroxene in the polar regions is in line with the results of the global spectral survey of 4506



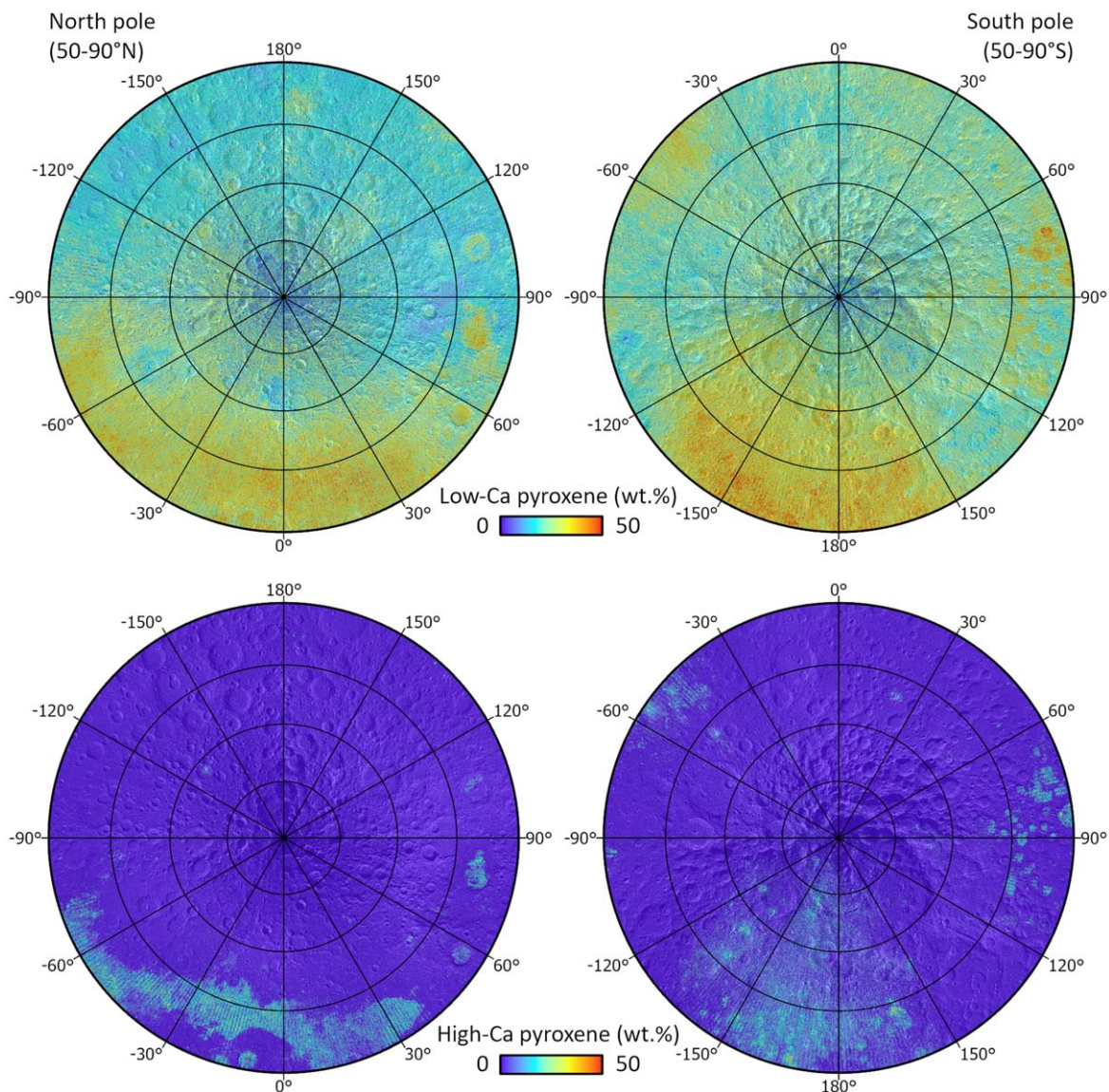


**Figure 10.** North and south polar maps of low- and high-calcium pyroxene abundances. The data are shown in polar stereographic projection between 50°–90°N (left) and 50°–90°S (right) in latitude with transparency over the Wide Angle Camera global mosaic.

immature, <1 km diameter craters conducted by Lucey et al. (2014) in the equatorial region ( $\pm 50^\circ$  in latitude) using Spectral Profiler data. Lucey et al. (2014) found that the small craters fall into three groups: (1) mare basalts with high ratios of high- to low-calcium pyroxene, (2) norites containing about 50 wt.% plagioclase and pyroxene assemblages dominated by low-calcium pyroxene (e.g., in SPA), and (3) noritic anorthosites containing about 20 wt.% low-calcium pyroxene in the highlands. Results from the polar regions are consistent with these observations.

High-calcium pyroxene is present in much lower abundances than low-calcium pyroxene and generally restricted to mare exposures and the center of SPA. This zone of increased high-calcium pyroxene in the center of SPA was also seen in the Kaguya Multiband Imager (Ohtake et al. 2014) and Moon Mineralogy Mapper (Moriarty & Pieters 2016) data and is commonly referred to as the Central SPA Compositional Anomaly (SPACA). Ohtake et al. (2014) suggested that it likely corresponds to impact melts (because it has a lower FeO abundance than the other mare regions in SPA) but could not

rule out the possibility that it can correspond to old mare deposits partially covered by ejecta from later impacts. Moriarty & Pieters (2016) suggested that it likely corresponds to resurfacing after the SPA impact melt sheet solidification. This resurfacing would be the result of volcanic flooding triggered in part by the SPA impact and distinct from later mare volcanism. In our case, we see similar mafic mineral abundances in SPACA and Mare Australe, which suggests that it likely represents volcanic flooding, although we cannot specify if it has been triggered by the SPA impact or corresponds to later mare volcanism.

The abundance of nanophase iron (Figure 11), which is responsible for the observed darkening and reddening of the lunar soil, is in excellent agreement with the observed 955.4/752.8 nm reflectance ratio (Figure 3). The abundance of nanophase iron is highest in the mare region on the near side and lower in the highlands. The lowest abundance is found within  $\sim 10^\circ$  in latitude of each pole.

Interpretation of mineral abundances derived using radiative transfer modeling can be best achieved with knowledge of the



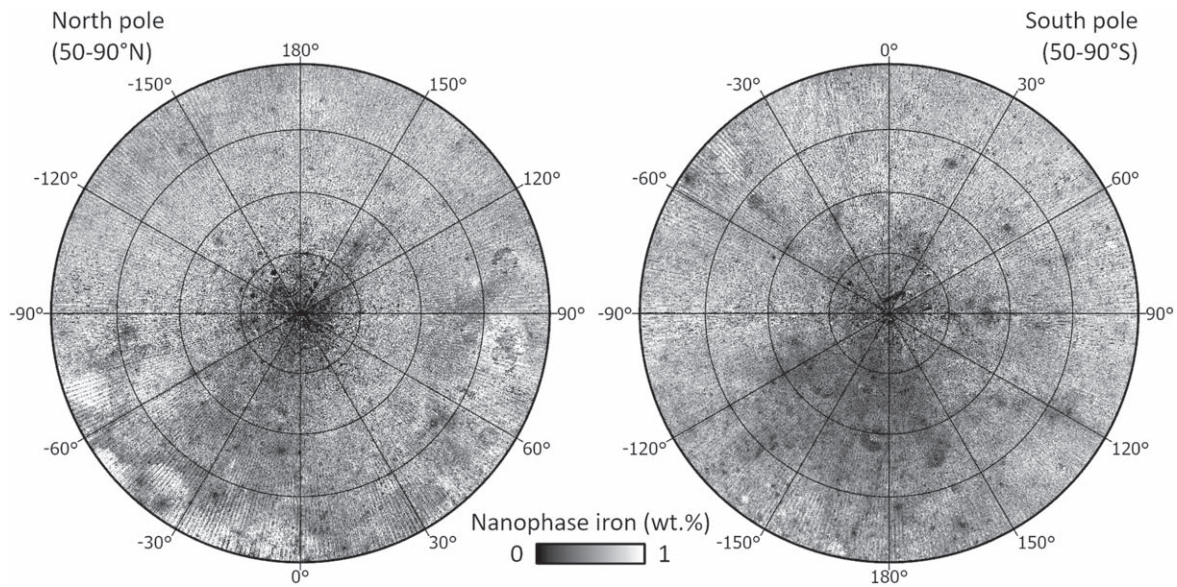


**Figure 11.** North and south polar maps of nanophase iron abundance. The data are shown in polar stereographic projection between 50°–90°N (left) and 50°–90°S (right) in latitude.

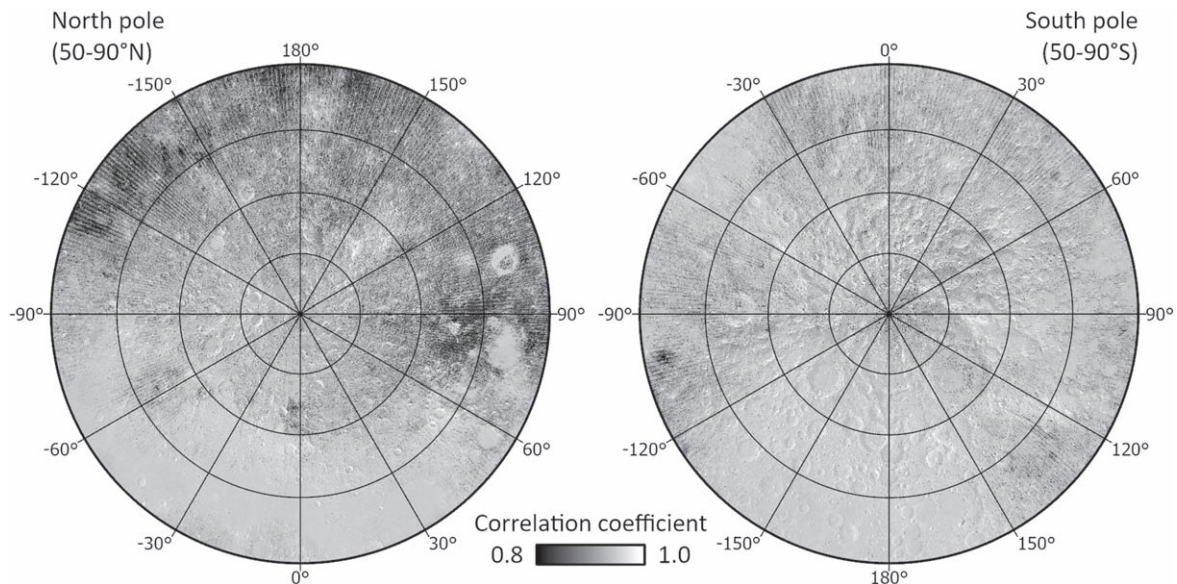


**Figure 12.** North and south polar maps of the correlation coefficient between the modeled and observed spectra. The data are shown in polar stereographic projection between 50°–90°N (left) and 50°–90°S (right) in latitude with transparency over the Wide Angle Camera global mosaic.

associated uncertainty. As mentioned previously, the optical constants used to model spectra herein yield an error (RMSE) of  $\sim 9$  wt.% in mineral abundance at the Spectral Profiler wavelengths (Figure 5). This uncertainty is perhaps smaller in practice when using the abundance of FeO in each pixel to ensure that the best-modeled spectral match contains stoichiometrically plausible FeO content. Nonetheless, as our model contains a defined set of elements, it can happen that the modeled spectra do not perfectly represent the spectra measured by the Spectral Profiler. Figure 12 presents the correlation coefficient between each best-modeled spectrum and the corresponding Spectral Profiler spectrum. In the north polar region, the mean correlation coefficient is 0.94. In the south polar region, the mean correlation coefficient is 0.97. Overall, better spectral matches are observed in the south polar

region than in the north. In the north polar region, the farside is generally characterized by lower correlation coefficients.

#### 6.4. Latitudinal Trend in Space Weathering and Optical Maturity

Using Clementine data, Hemingway et al. (2015) discovered an increase in albedo with latitude in the maria. They proposed that this increase in reflectance could be attributed to solar wind flux, which depends on latitude, as a known agent of space weathering. Lemelin et al. (2016) confirmed this observation using LOLA normal albedo data and confirmed that this variation is not an artifact arising from the distribution of compositions within the lunar maria. A strong relationship between the average solar flux and LOLA normal albedo data was observed. This relationship was the strongest in the maria

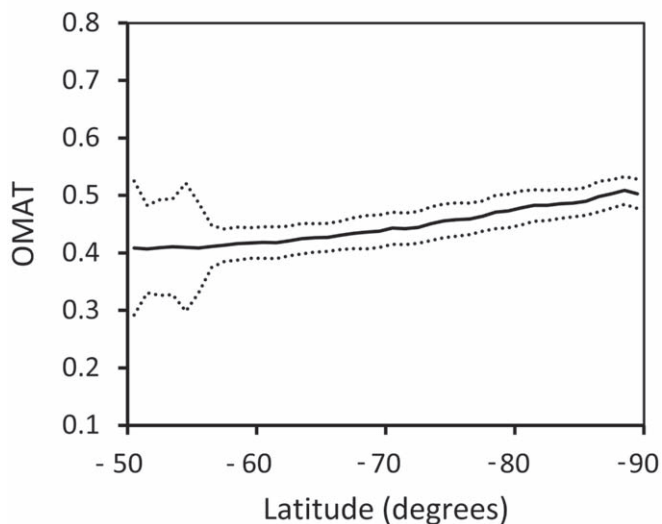
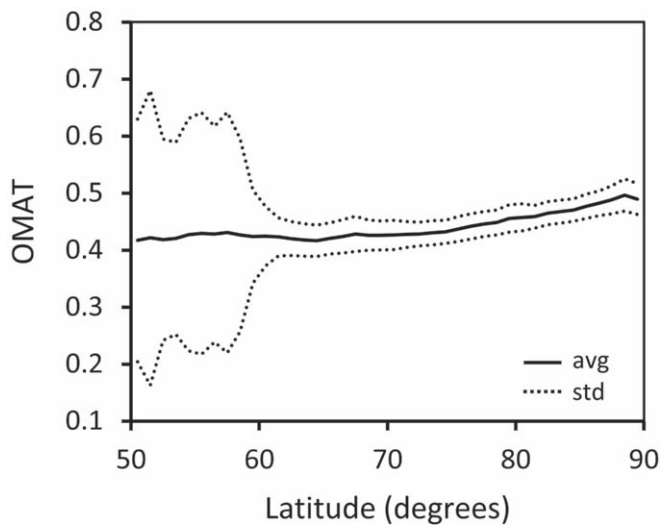


**Figure 13.** Average OMAT value by latitude for each polar region. The OMAT values analyzed are constrained to sunlit and nearly flat surfaces with slopes shallower than  $5^\circ$ . In both polar regions, the OMAT values display a steady increase poleward of  $\sim 60^\circ$ , reaching a high of  $\sim 0.5$  near both poles.

but appeared to also be weakly present in the highlands. Lemelin et al. (2016) used a radiative transfer model and Multiband Imager data (within  $\pm 50^\circ$  of latitude) to investigate if the increase in reflectance with latitude is related to the abundance of nanophase and/or microphase iron, which are solar wind-related space weathering products. They found that indeed, the abundance of nanophase iron is dependent on the average solar flux. The microphase abundance they modeled appeared to be influenced by the presence of opaque minerals due to their model formulation, so they did not proceed with further analysis on this data set. Here we use the newly mapped OMAT (Figure 13) and nanophase iron (Figure 14) products to extend the observation of space weathering up to the poles. In both cases, we constrain our observation to sunlit and nearly flat surfaces with slopes shallower than  $5^\circ$ . For nanophase iron, we additionally constrain our observations to the feldspathic highlands terrane, surfaces with FeO content lower than 10 wt. %. In both polar regions, OMAT values display a steady increase poleward of  $\sim 60^\circ$ , reaching a high of  $\sim 0.5$  near both poles (Figure 13). Similarly, in both polar regions, nanophase

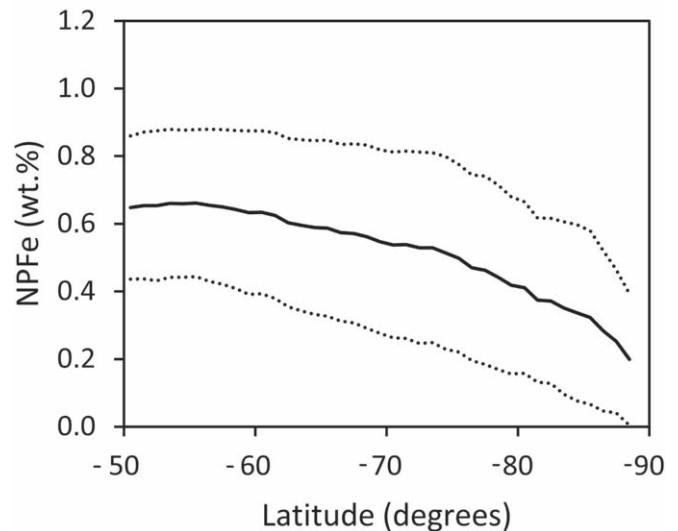
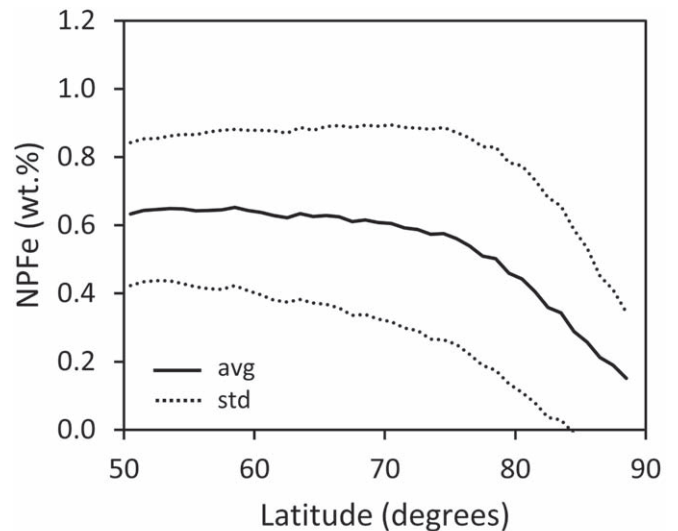


**Figure 14.** Average abundance of nanophase iron (NPF) by latitude for each polar region. The nanophase iron values analyzed are constrained to sunlit, nearly flat surfaces (slopes shallower than  $5^\circ$ ) and surfaces with FeO content lower than 10 wt. %. In both polar regions, nanophase iron abundances display a steady decrease poleward of  $\sim 60^\circ$ – $70^\circ$ , reaching a low of  $\sim 0.2$  wt. % near both poles. Nanophase iron is approximately three times less abundant at the poles than in the equatorial region ( $\sim 50^\circ$ – $60^\circ$ ).

iron abundances display a steady decrease poleward of  $\sim 60^\circ$ – $70^\circ$ , reaching a low of  $\sim 0.2$  wt. % near both poles (Figure 14). Nanophase iron is approximately three times less abundant at the poles than in the equatorial region ( $\sim 50^\circ$ – $60^\circ$ ).

### 6.5. Characterization of the Artemis Region

The Artemis III mission, part of the Artemis program put forward by NASA, aims to send humans to the lunar surface by  $\sim 2025$ . The Artemis III mission is targeting to land in the south polar region of the Moon, more precisely between  $84^\circ$  and  $90^\circ$  S (the so-called Artemis region). The precise landing site has not been determined, but six regions of interest have been identified. These regions are located near permanently shadowed regions, which may contain volatiles. These regions may also offer long-duration access to sunlight, direct-to-Earth communication, and surface slopes and roughness favorable for landers and astronauts (NASA 2020).



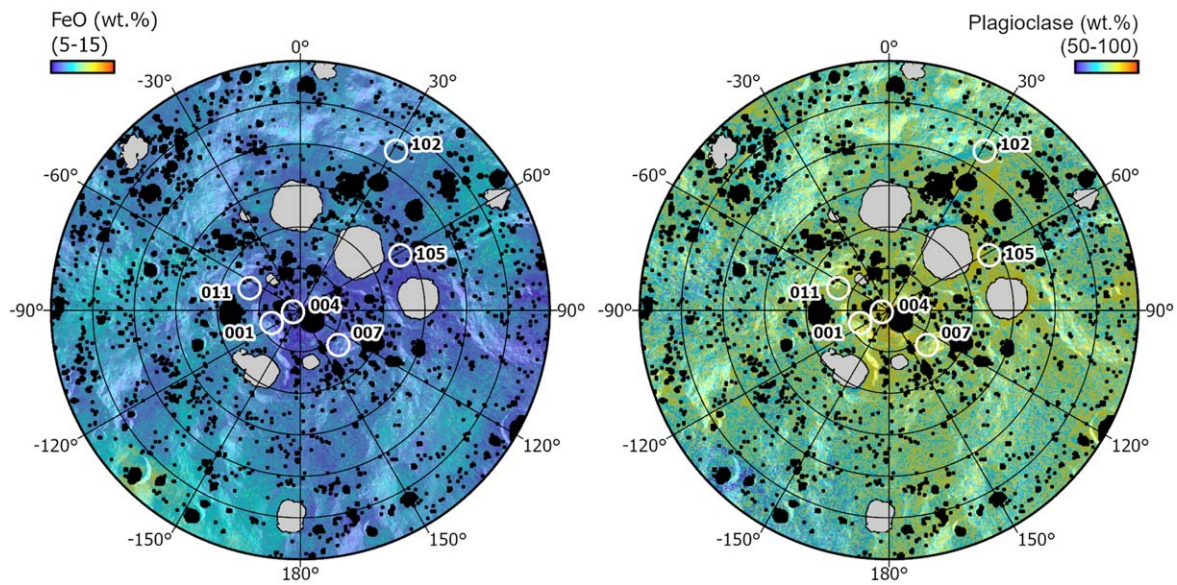


**Figure 15.** Iron and plagioclase content of the Artemis region (84°–90°S). Black polygons represent permanently shaded regions from Mazarico et al. (2011), while gray polygons represent the 11 water ice-bearing permanently shaded regions identified by Lemelin et al. (2021) as high-priority exploration sites. The six potential Artemis sites identified by NASA (2020) are shown as white circles.

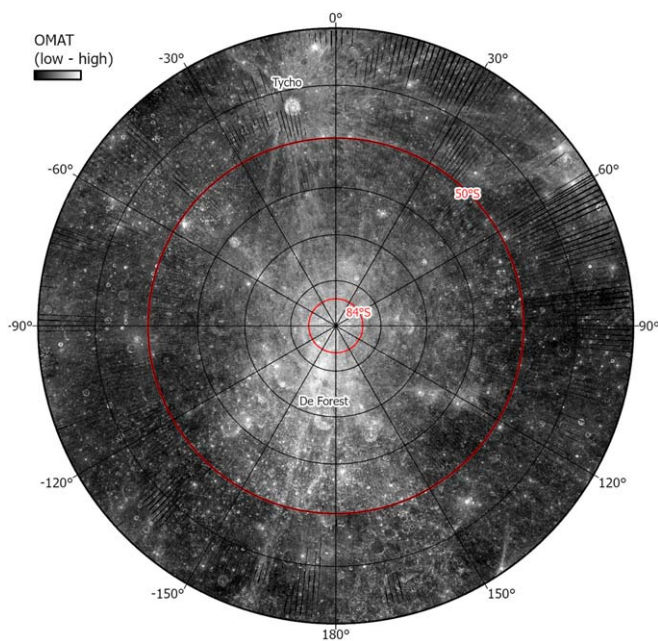


**Figure 16.** Optical OMAT of the south polar and Artemis regions (84°–90°S). Bright OMAT rays extend from Tycho and De Forest craters into the Artemis region. OMAT values between 30° and 50°S are derived from the Kaguya Multiband Imager data (Lemelin et al. 2019), and OMAT values between 50° and 90°S are derived from the Kaguya Spectral Profiler data herein.

The mineral maps produced herein suggest that the Artemis region is characterized by relatively homogeneous FeO (~5–10 wt%) and plagioclase (~80–90 wt%) content at the observed spatial resolution of 1 km pixel<sup>-1</sup> (Figure 15). The lowest FeO values (~5–7 wt.%) are found in the 89°–90°S region near Shackleton crater, between Shoemaker and Faustini craters, as well as on the central peak of Amundsen crater. A few exposures of anorthosites (>90 wt.% plagioclase) are concentrated around Shackleton crater (89°9S) and on or near the ridge between Shackleton and Henson crater (~88°5S, 128° W). Exposures of pure anorthosites (≥98 wt.% plagioclase)

were seen in individual Spectral Profiler spectra (spatial resolution of 500 m pixel<sup>-1</sup>) by Yamamoto et al. (2012) and Lemelin et al. (2017) on the rim of Shackleton crater (close to Artemis site 004) but are not seen in the gridded (1 km pixel<sup>-1</sup>) data. Our new polar OMAT data suggest that rays coming from Tycho crater may extend up to the south pole and are low in optical maturity (high OMAT values; Figure 16). The brightest ray appears to drape the region between Artemis sites 001 and 004. This region was recently mapped by Speyerer et al. (2016). The crater De Forest (77°3S, 162°1W) also seems to have excavated and distributed fresh material in the Artemis region. The entire Artemis region is, however, characterized by high OMAT values, which complicates the identification of the precise contribution of each crater to the high OMAT values. Overall, the mineral maps derived herein offer a first compositional view of the Artemis region. However, considerable efforts should be taken to derive similar maps at higher spatial resolution to guide upcoming robotic and human missions. Data acquired by instruments such as the Imaging Infrared Spectrometer on board the current Chandrayaan-2 mission or the High-resolution Volatiles and Minerals Moon Mapper on board the upcoming Lunar Trailblazer mission could be used in the near future. These data sets offer a spatial resolution of 70–80 m pixel<sup>-1</sup>, which could allow one to drastically increase the spatial resolution of the derived mineralogical maps and consequently identify smaller lithologies (such as the pure anorthosites).

## 7. Conclusion

We generated an absolute reflectance data cube from the Kaguya Spectral Profiler data set and used it to derive the first quantitative mineral maps of iron oxide (FeO), the optical maturity parameter (OMAT), and nanophase iron poleward of 50°N/S at a spatial resolution of 1 km pixel<sup>-1</sup>. We evaluated potential latitudinal trends in space weathering and optical maturity and characterized the polar geology, with an emphasis on the Artemis region (84°–90°S).

We find that the maps of FeO are in excellent agreement with the abundances measured by the Lunar Prospector and provide an increased level of detail, such as the excavation of high- and low-FeO material by De Forest crater. The OMAT maps offer a fantastic view of both polar regions. They highlight small fresh craters, fresh walls, and central peaks, as well as rays extending through multiple degrees of latitude, such as those from Tycho and De Forest, which extend into the Artemis region, likely between Artemis sites 001 and 004. Both polar regions are characterized by the ubiquitous presence of noritic anorthosites and anorthositic norite. Low-calcium pyroxene is largely the dominant mafic mineral present. The Artemis region appears to be characterized by relatively homogeneous FeO and plagioclase content at the observed spatial resolution. The lowest FeO values are found in the 89°–90°S region around Shackleton crater, between Shoemaker and Faustini craters, as well as on the central peak of Amundsen crater. The 1 km gridded data cube does not allow one to resolve the exposures of pure anorthosite seen on the rim of Shackleton crater by Yamamoto et al. (2012) and Lemelin et al. (2017). Data acquired by instruments such as the Imaging Infrared Spectrometer on board the Chandrayaan-2 mission or the High-resolution Volatiles and Minerals Moon Mapper on board the upcoming Lunar Trailblazer mission could be used in the near future to refine the level of detail currently identifiable, such as these localized lithologies.

This research was undertaken, in part, thanks to funding from the Canada Research Chair in Northern and Planetary Geological Remote Sensing and an NSERC Discovery grant held by M.L. The work conducted by P.G.L. in this project was supported by NASA Planetary Data Archiving, Restoration, and Tools (PDART) grant No. NNX17AK92G. The reflectance and compositional mosaics derived in this study can be found in Zenodo:10.5281/zenodo.5847000. The authors would like to sincerely thank the reviewers for their comments, which enhanced the quality of the presented work.

### ORCID iDs

Myriam Lemelin  <https://orcid.org/0000-0002-3952-8086>  
Paul G. Lucey  <https://orcid.org/0000-0002-4959-2495>

### References

Barker, M. K., Sun, X., Mazarico, E., et al. 2016, *Icar*, 273, 96  
Britt, D. T., & Pieters, C. M. 1994, *GeCoA*, 58, 3905

Cheek, L. C., Donaldson Hanna, K. L., Pieters, C. M., et al. 2013, *JGRE*, 118, 1805  
Crites, S. T., Lucey, P. G., & Taylor, G. J. 2015, *AmMin*, 100, 1708  
Hapke, B. 1981, *JGR*, 86, 3039  
Hapke, B. 1993, *Topics in Remote Sensing*, (Cambridge: Cambridge Univ. Press)  
Hapke, B. 2001, *JGR*, 106, 10039  
Haruyama, J., Matsunaga, T., Ohtake, M., et al. 2008, *EP&S*, 60, 243  
Haruyama, J., Yamamoto, S., Yokota, Y., et al. 2013, *GeoRL*, 40, 3814  
Hemingway, D. J., Garrick-Bethell, I., & Kreslavsky, M. A. 2015, *Icar*, 261  
ISECG 2018, The Global Exploration Roadmap NP-2018-01-2502-HQ, NASA, [https://www.globalspaceexploration.org/wordpress/wp-content/isecg/GER\\_2018\\_small\\_mobile.pdf](https://www.globalspaceexploration.org/wordpress/wp-content/isecg/GER_2018_small_mobile.pdf)  
ISECG 2020, The Global Exploration Roadmap Supplement August 2020, Lunar Surface Exploration Scenario Update NP-2020-07-2888-HQ, NASA, [https://www.globalspaceexploration.org/wp-content/uploads/2020/08/GER\\_2020\\_supplement.pdf](https://www.globalspaceexploration.org/wp-content/uploads/2020/08/GER_2020_supplement.pdf)  
Kramer, G. Y., Kring, D. A., Nahm, A. L., et al. 2013, *Icar*, 223, 131  
Lawrence, D. J., Feldman, W. C., Elphic, R. C., et al. 2002, *JGR*, 107, 5130  
Lemelin, M., Li, S., Mazarico, E., et al. 2021, *PSJ*, 2, 103  
Lemelin, M., Lucey, P. G., Jha, K., & Trang, D. 2017, *LPSC*, 48, 2479  
Lemelin, M., Lucey, P. G., Miljkovic, K., et al. 2019, *P&SS*, 165, 230  
Lemelin, M., Lucey, P. G., Neumann, G. A., et al. 2016, *Icar*, 273, 315  
Lemelin, M., Lucey, P. G., Song, E., & Taylor, G. J. 2015, *JGRE*, 120, 869  
Li, S., Lucey, P. G., Fraeman, A. A., et al. 2020, *SciA*, 940, eaba1940  
Lucey, P. G. 1998, *JGR*, 103, 1703  
Lucey, P. G. 2004, *GRL*, 31, L08701  
Lucey, P. G. 2006, *JGR*, 111, E08003  
Lucey, P. G., Blewett, D. T., & Hawke, B. R. 1998, *JGR*, 103, 3679  
Lucey, P. G., Blewett, D. T., Taylor, G. J., & Hawke, B. R. 2000, *JGR*, 105, 20377  
Lucey, P. G., & Noble, S. K. 2008, *Icar*, 197, 348  
Lucey, P. G., Norman, J. A., Crites, S. T., et al. 2014, *AmMin*, 99, 2251  
Lucey, P. G., & Riner, M. A. 2011, *Icar*, 212, 451  
Lucey, P. G., Taylor, G. J., & Malaret, E. 1995, *Sci*, 268, 1150  
Mazarico, E., Neumann, G. A., Smith, D. E., Zuber, M. T., & Torrence, M. H. 2011, *Icar*, 211, 1066  
Moriarty, D. P., III, & Pieters, C. M. 2016, *LPSC*, 47, 1735  
Moriarty, D. P., III, & Pieters, C. M. 2018, *JGRE*, 123, 729  
Moriarty, D. P., III, Watkins, R. N., & Petro, N. E. 2020, *LPI Contribution*, 2241, 5152  
Morris, R. V. 1978, *LPSC*, 9, 2287  
NASA 2020, NASA's Plan for Sustained Lunar Exploration and Development, [https://www.nasa.gov/sites/default/files/atoms/files/a\\_sustained\\_lunar\\_presence\\_nspc\\_report4220final.pdf](https://www.nasa.gov/sites/default/files/atoms/files/a_sustained_lunar_presence_nspc_report4220final.pdf)  
Noble, S. K., Pieters, C. M., & Keller, L. P. 2007, *Icar*, 192, 629  
Ohtake, M., Uemoto, K., Yokota, Y., et al. 2014, *GeoRL*, 41, 2738  
Pieters, C. M., Fisher, E. M., Rode, O., & Basu, A. 1993, *JGR*, 98, 20817  
Smith, D. E., Zuber, M. T., Jackson, G. B., et al. 2010, *SSRv*, 150, 209  
Speyerer, E. J., Lawrence, S. J., Stopar, J. D., et al. 2016, *Icar*, 273, 337  
Taylor, L. A., Pieters, C. M., Keller, L. P., Morris, R. V., & McKay, D. S. 2001, *JGR*, 106, 27985  
Yamamoto, S., Matsunaga, T., Ogawa, Y., et al. 2011, *ITGRS*, 49, 4660  
Yamamoto, S., Matsunaga, T., Ogawa, Y., et al. 2014, *ITGRS*, 52, 6882  
Yamamoto, S., Nakamura, R., Matsunaga, T., et al. 2010, *NatGe*, 3, 533  
Yamamoto, S., Nakamura, R., Matsunaga, T., et al. 2012, *GeoRL*, 39, L13201  
Yokota, Y., Matsunaga, T., Ohtake, M., et al. 2011, *Icar*, 215, 639